Author Manuscript

Seasonal variability of internal tides and associated energy budget over the eastern Arabian Sea: Observations and Modelling

Pragnya Makar[1], A.D. Rao[1], B. Yadidya[2], and Vimlesh Pant[1]

[1]Centre for Atmospheric Sciences, Indian Institute of Technology Delhi, New Delhi, India.

[2] Department of Earth & Environmental Sciences, University of Michigan, Ann Arbor, MI, USA

Key Points:

- The study provides a detailed analysis of the seasonal variability of diurnal and semidiurnal internal tides in the eastern Arabian Sea
- Internal tide generation is higher in the north during pre-monsoon and in the south during monsoon due to stronger stratification
- Energy budget analysis shows strong seasonal variation at generation sites, with variability up to 1.03 GW in the Maldives region.

Abstract

The seasonal variability of internal tides in the Eastern Arabian Sea was studied in detail using *in-situ* observations and numerical modeling. Moored buoy observations identified M_2 and K_1 as the predominant tidal constituents, succeeded by S_2 and O_1. The 3D- Massachusetts Institute of Technology General Circulation Model is used to study the seasonal changes in the generation, propagation, and dissipation of internal tides. We found that internal tides are primarily generated along the continental shelf-slope break, with prominent generation sites off Mumbai in the north, around the Lakshadweep region, and near the Maldives in the south. Stratification varies both seasonally and regionally, strengthening from north to south. The enhancement of internal tide available potential energy and horizontal kinetic energy is observed during the pre-monsoon season in the north and during the monsoon season in the south, attributed to increased stratification. Shelf-slope areas off Mumbai and near the Maldives contribute approximately 66% of the total barotropic-to-baroclinic energy conversion. Energy flux patterns indicate a southwestward propagation from the Mumbai region and a westward propagation from the Maldives. Semidiurnal energy conversion and associated fluxes generally exceed those of diurnal energy across most seasons. These findings underscore that seasonal variability is primarily driven by changes in stratification, offering essential insights into the dynamics of internal tides in this region.

Plain Language Summary

This study explores the seasonal changes in internal tides in the Eastern Arabian Sea using measurements from ocean buoys and computer modeling. Internal tides are underwater waves generated by tidal forces and are important because they help mix ocean waters, affecting ocean life and climate. We found that the main types of tidal waves in this region are the M_2 and K_1 tides. These internal tides are mostly generated along the edges of the continental shelf, particularly near Mumbai, the Lakshadweep region, and the Maldives. Seasonal and regional

This is the author manuscript accepted for publication and has undergone full peer review but has not been through the copyediting, typesetting, pagination and proofreading process, which may lead to differences between this version and the Version of Record. Please cite this article as doi: 10.1029/2024JC021529.

This article is protected by copyright. All rights reserved.

Author Manuscript

changes in ocean density stratification influence these internal tides, with stronger layering found in the south. The strongest generation of internal tides occurs in spring and summer, and most of the energy from these waves moves southwest from Mumbai and westward from the Maldives. The highest internal tide activity is observed during the pre-monsoon season in the north and the monsoon season in the south, primarily due to stronger stratification. Our findings show that changes in stratification across seasons are key drivers of internal tides in this area, helping us better understand the seasonal behavior and impact of these underwater waves.

1 Introduction

Internal tides (ITs) are internal waves at tidal frequencies that propagate in the stratified ocean (Wunsch, 1975). The ITs are produced when barotropic tides interact with topographic features such as mid-oceanic ridges, continental slopes, shelf breaks, and so on in the presence of stratification (Garrett & Kunze, 2007). These waves in the shelf-slope region play a significant role in energy transfer through ocean mixing, impacting density structure, submarine acoustics, and offshore structures (Mohanty, 2018). An estimated 3.7 terawatts (TW) of energy is generated by astronomical tides, with about 3.5 TW dissipated within the oceans (Munk & Wunsch, 1998). Egbert and Ray (2000) suggested that roughly one TW tidal power is converted from barotropic tides into IT in the deep ocean, while the remaining 2.5 TW of tidal energy is dispersed in shallow waters.

The eastern part of the Arabian Sea (EAS) undergoes seasonal variations in numerous processes, which have a significant impact on its physical and dynamical characteristics. The ITs in the EAS region holds significance in understanding acoustic propagation for the naval operations, health of the coral reefs around the Lakshadweep and Maldives islands, and oil and gas drilling operations off Mumbai coast, etc. Unlike the eastern boundary currents of other oceans, the EAS shows marked seasonal changes in its currents due to reversal of monsoonal winds. The West Indian Coastal Current (WICC) plays a crucial role in governing the circulation within this region. The WICC has a northward flow during the winter monsoon spanning from November to February. While in the summer monsoon, covering from June to September, the WICC demonstrates an equatorward flow (Shetye et al., 1991). During the inter-monsoon period (March to April and October to November), weak and highly variable wind regimes occur, and the basin-scale features of the circulation dissipate (Gangadhara Rao & Shreeram, 2005). At the time of formation of northward current during winter, a high in the sea level known as Lakshadweep high forms between Lakshadweep Sea and the southeast AS, which migrates westwards. Similarly, Lakshadweep low forms when WICC is equatorward

This article is protected by copyright. All rights reserved.

during summer (Shetye, 1998). The AS has a complex tidal system, with diurnal, semidiurnal, and mixed tide components that are equally significant. India's west coast is characterized by a narrow continental shelf that stretches from about 85 km in the south at 9°N to about 230 km in the north at 20°N (Subeesh et al., 2013). The tidal range undergoes an amplification from 0.8 m to 5 m as it covers from the southern tip to northern part of the Indian coast due to the widening of the shelf. The continental shelf opens into the Gulf of Khambhat (near the latitude of 21ºN), which experiences the second highest tidal range in the world, measuring approximately 11-12 meters. This phenomenon is attributed to the combination of the funneling effect and the shallow depth of the gulf. During the summer monsoon, regions of coastal upwelling are generally observed along the southeastern AS due to favorable alongshore wind stress acting upon the sea-surface with the coast to its left. This results in a reduction of sea surface temperature with shoaling of isotherms and lowering of sea level (Joseph et al., 2019). During spring-summer transition (April-May), formation of a mini warm pool is observed over the southeast AS with a maximum sea surface temperature of about 32ºC, which may enhance development of the monsoon onset vortex (Rao & Sivakumar, 1999). Surface advection of cold and less saline Bay of Bengal (BoB) waters over the warm saline AS waters is observed during the winter monsoon. Thadathil and Gosh (1992) found that presence of low-salinity waters in the surface layer of the southern EAS, which acts as a barrier layer for the formation of temperature inversions in the region.

Vertical stratification of the ocean waters is necessary and a prerequisite for the existence of internal wave in any oceanic region. A change in stratification leads to a change in internal wave activity at the subsurface (Chuang and Wang., 1981; Mohanty et al., 2019; Yadidya & Rao, 2022b) . The internal tidal wave energy is linked to a downwelling-favorable wind event, which weakened stratification by increasing vertical mixing and moving deeper water away from the continental shelf (Sharples & Zeldis, 2019). As previously discussed, the seasonal events occurring in the EAS are expected to influence the seasonal variability of internal wave activity, primarily through changes in stratification. Although there has been some research conducted in the BoB and the Andaman Sea, there is a limited knowledge regarding the variability of ITs in the EAS. Rao et al. (2010) used a three-dimensional Princeton Ocean Model (POM) to investigate formation of internal wave in the western BoB. The study underlines that low frequency ITs have the most energy and that the model can reasonably reproduce the diurnal and semidiurnal components up to 6 hours. Pradhan et al. (2014; 2016) used the Massachusetts Institute of Technology general circulation model (MITgcm) to

This article is protected by copyright. All rights reserved.

Author Manuscript

Author Manuscript

simulate ITs over the BoB and have shown interseasonal variability of IT and its characteristics on different gradients of continental shelves varying from 0.2° to 0.5°. The findings showed that the peak of IT activity changes spatially throughout the continental shelf and a concave shoreline coast has more energy than a straight coastline, implying that IT energy is converging towards the concave coast. Mohanty et al. (2019) made numerical simulations using MITgcm and found that IT is generated all along the east coast over the shelf-slope zone and that the energy is confined near Machilipatnam due to the crescent shape of the local coastal geometry. Study conducted by Mohanty et al. (2017; 2018) delved into the energetics of semidiurnal ITs over the western BoB and Andaman Sea using 3D MITgcm model. They examined the generation, propagation, and dissipation patterns of IT over the eastern side of the Indian Peninsula and highlighted that the northern BoB experiences the highest activity of ITs. Furthermore, the Andaman Sea stands out for its notably higher observed amplitudes of ITs, indicating a pronounced presence of energetic internal tidal phenomena in this region. Notably, the study revealed that the baroclinic energy of IT dissipates locally, and the conversion of energy from barotropic to baroclinic is notably greater in the Andaman Sea compared to that of the BoB. Yadidya et al. (2022a) showed that the kinetic energy of semidiurnal IT is dominant over that of diurnal IT over the Andaman Sea by a factor of 4 to 5. Further, it is concluded that the Andaman Nicobar Ridge is responsible for about 89% of the overall IT generation. According to Yadidya and Rao (2022c), the Andaman Sea is projected to experience an increase in depth-averaged stratification by approximately 6% under the SSP1-2.6 scenario, 7% under SSP2-4.5, and 12% under SSP5-8.5, when comparing the periods 1871–1900 to 2081–2100. This projected intensification of stratification is anticipated to significantly enhance the generation of ITs.

Extensive research has been conducted in the BoB and the Andaman Sea, where semidiurnal tides dominate. On the other hand, the AS displays a combination of semidiurnal, diurnal, and mixed tides. The temperature is a primary determinant in the stratification of the AS, with salinity also exerting a notable influence in the southeastern area.

However, studies of IT in the EAS, on the other hand, have received little attention. Hareesh et al. (2010) showed the existence of high frequency internal wave and semi-diurnal IT by analyzing high-frequency time-series data of temperature and salinity collected at a location in the EAS. Using observed currents from Acoustic Doppler Current Profiler (ADCP) over the continental shelf at five different locations along the west coast of India, Subeesh et al. (2013) noticed that the amplitudes of both semidiurnal and diurnal IT increase as the stratification

This article is protected by copyright. All rights reserved.

Author Manuscript

along the shelf strengthens from the pre-monsoon to the southwest monsoon period. Subeesh and Unnikrishnan (2016) focused on the region off south of Mumbai, considering two locations at the shelf break and the shelf-slope region. The study observes peaks in the baroclinic current spectra of horizontal velocities at frequencies corresponding to M_2, S_2, K_1, O_1, and the inertial frequency (*f*). It is also reported that the strength of barotropic tidal currents and IT along the northern part of the shelf slope are dominant, influencing the observed current variability. Ma et al. (2021) utilizing sea-level anomaly data collected by the satellite altimeter showed that the energy flux of ITs during winter is high compared to that in summer in the northeastern AS. Kaur and Buijsman (2022) analyzed six years of HYCOM model simulations and found that the AS shows the largest seasonal stationary (coherent) variance fraction of semidiurnal constituent M_2 among other oceans in the world. Using the Regional Ocean Modelling System (ROMS), Subeesh et al. (2021) demonstrated that the M_2 internal tides are generated significantly in two regions in the EAS: between 16°–18.5° N, and the Chagos-Laccadive Ridge between 8-12°N. The study uncovers that the central and northern slope regions off the west coast of India, which are mainly influenced by the locally generated ITs. However, in the southern region, the ITs are also caused by the presence of remotely generated IT originating from the Islands. Ma et al. (2023) also utilized the MITgcm model for the entire AS to simulate IT for January and July, representing winter and summer seasons respectively. They demonstrated that the ITs in the AS are more pronounced in January.

No modelling study in the past is reported to study a comprehensive mechanism of IT that includes generation, propagation, and dissipation on a seasonal basis along with baroclinic tidal energy budget in the regions where the ITs are predominantly observed. In the present study, we initially use time-series observations collected from the moored buoys located in the EAS to understand IT characteristics by analyzing it. The MITgcm is also used to validate its simulations with observations. The model identifies the regions of generation, propagation and energy dissipation of IT during January, April, July, and October representing respectively winter, pre-monsoon, monsoon, and post-monsoon seasons. The baroclinic tidal energy budget is quantified in the regions where the ITs are prevalent. This study is the first of its kind to provide a deep insight into the characteristics of IT at semidiurnal and diurnal frequencies and its seasonal variability in the EAS.

2 Data and Methodology

This article is protected by copyright. All rights reserved.

Author Manuscript

The Ocean Moored Network for the Northern Indian Ocean (OMNI), consisting of moored buoys, has been in service since October 2012. The National Institute of Ocean Technology, India has put up moored buoys, AD08 at (12°N, 68.65°E), AD09 at (8.22ºN, 73.28ºE), and AD10 at (10.34ºN,72.58ºE), where the local depths are about 4300m, 2200m and 1800m respectively as shown in Figure 1. The sensors used for these observations are elaborated by Venkatesan et al. (2013). Hourly measurements of temperature and conductivity were collected at different depths (1, 5, 10, 15, 20, 30, 50, 75, 100, and 200 m). The ADCP was used to measure the speed and direction of currents at depths ranging from 15 to 150 meters at AD08, AD09 and AD10. Hourly observations are available at every 5m in the vertical. The model validation is also performed with the buoy data obtained from the Research Moored Array for African-Asian-Australian Monsoon Analysis and Prediction (RAMA; McPhaden et al., 2009) located at (15.14°N, 65.10°E) (ID No. 2300011). In this case, the temperature and salinity data are available from 19th June 2018 to 21st October 2020. The local depth at this location is about 3850 m and the data is available at depths, specifically at 1, 5, 10, 20, 40, 60, 100, and 140m.

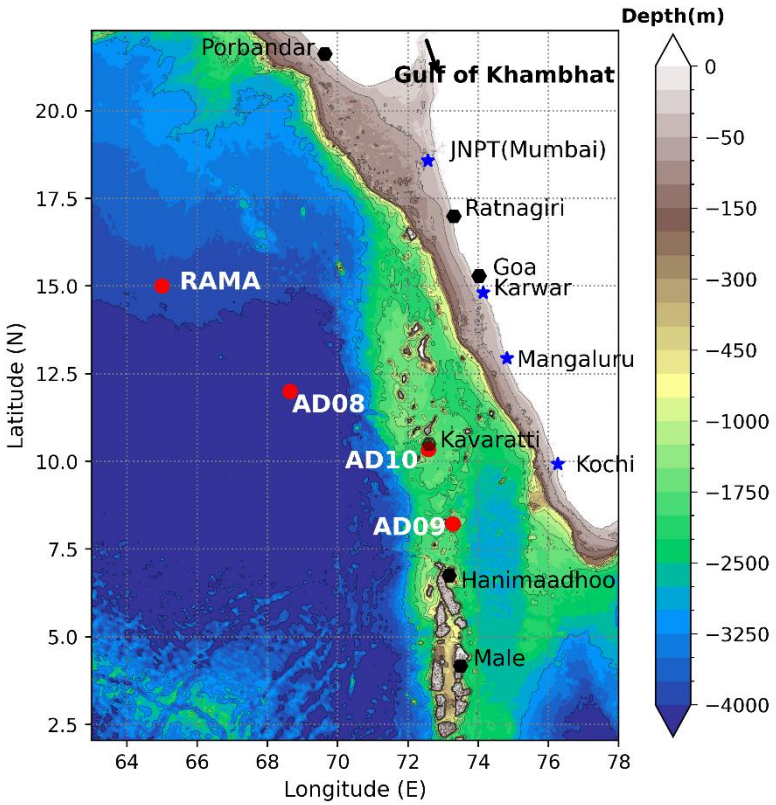

Figure 1. Model domain with bathymetry (●) represents location of the buoys (★) represents tide-gauge locations (⬣) represents coastal cities.

This article is protected by copyright. All rights reserved.

Author Manuscript

As the ADCP data did not cover the entire local depth, the barotropic currents are calculated using TOPEX/Poseidon global tidal model (TPXO9.2) OSU Tidal Prediction Software (OTPS) for observational analysis (Egbert & Erofeeva, 2002). Barotropic currents are subtracted from the raw currents to compute the baroclinic currents. Using a fourth-order Butterworth filter to bandpass time series baroclinic current and distinguish between diurnal (0.8–1.2 cpd) and semidiurnal (1.8–2.2 cpd) frequency.

The baroclinic equation with depth-integrated and time averaging is as follows (Buijsman et al., 2012; Yadidya et al., 2022a)

$$\langle \nabla . F \rangle = \langle C \rangle - \langle D \rangle$$

where, $\nabla . F$ is the depth-integrated divergence of baroclinic tide energy flux, C is the depth-integrated barotropic to baroclinic conversion energy, D is the depth-integrated dissipation of baroclinic tide energy. The 14-day average shown in the angle bracket eliminates the impact of intra-tidal and neap-spring variation. Barotropic to baroclinic energy conversion is estimated using the equation (Yadidya et al., 2022a),

$$C = g \int_{-H}^{\eta} \rho' w_{bt} dz$$

where, g is the acceleration due to gravity, ρ' represents the density perturbation, w_{bt} is the barotropic vertical velocity, H and η are the time-mean water depth and surface tidal elevation, respectively.

Baroclinic tidal flux (F) is calculated from the covariance between baroclinic tidal velocity (u') and pressure perturbation (p'), by considering hydrostatic assumption (Kunze et al., 2002). Since IT frequencies are much lower than the buoyancy frequency, the hydrostatic assumption is generally valid. Depth-integrated IT energy flux can be estimated using the following relation given by Kunze et al. (2002)

$$\nabla . F = \nabla_h . \left[\int_{-H}^{\eta} u' p' \, dz \right]$$

where, the pressure perturbations are computed as

$$p'(z,t) = -\frac{1}{H} \int_{-H}^{\eta} \int_{z}^{\eta} g\rho'(\hat{z},t) d\hat{z} \, dz + \int_{z}^{\eta} g\rho'(\hat{z},t) d\hat{z}$$

Depth-integrated energy density (E) is the sum of Horizontal Kinetic Energy (HKE) and Available Potential Energy (APE), which are given by

This article is protected by copyright. All rights reserved.

$$HKE = \frac{\rho_0}{2}\int_{-H}^{0} \langle |u'(z,t)|^2 \rangle \, dz \quad \text{and} \quad APE = \frac{g^2 \rho'^2}{2\rho_0 N^2}$$

where, ρ_0 is the reference water density, $N^2 = \frac{-g}{\rho_0}\frac{\partial \rho}{\partial z}$ is the buoyancy frequency, ρ is the instantaneous density.

2.1 Model Configuration

This study employs the 3D- Massachusetts Institute of Technology general circulation model (MITgcm) developed by Marshall et al. (1997) (http://mitgcm.org/), which is configured for the EAS. The 3D-MITgcm is a *z*-coordinate finite-volume model that has the capability to be either hydrostatic or non-hydrostatic. However, we use hydrostatic version of the model in the present study. The model solves the incompressible Navier-Stokes equations, by employing the Boussinesq approximation and utilizing an Arakawa-C grid. The study encompasses a model domain ranging from 2°N to 22°N and 63°E to 78°E, as shown in Figure 1. The horizontal grid resolution is about 2.7 km. The model bathymetry is derived from the General Bathymetric Chart of the Oceans (GEBCO_2023) (https://www.gebco.net) with a horizontal resolution of 15 arc-sec interval grid, as depicted in Figure 1. The model grid consists of 47 vertical levels with a resolution of 5 m up to upper 150 m, and then increases slowly to a course resolution. At the bottom boundary, a no-slip condition is enforced, while free-slip condition is applied at the lateral boundaries. The Smagorinsky formulation (Smagorinsky, 1963) is used to parameterize the horizontal eddy viscosity and diffusivity, While the K-profile parameterization (Large et al., 1994) is used to parameterize the vertical eddy viscosity and diffusivity. The beta-plane approximation is made to take care of the change in Coriolis parameter with latitude. The model time step is considered as 120 sec based on Courant–Friedrichs–Lewy criteria. A sponge layer of grid point 8 is used to prevent reflection of ITs near the boundaries. This study incorporates hourly specific humidity, air temperature at 2 m above the surface, wind speed at 10 m above sea level, and mean surface net longwave and shortwave radiation flux, runoff, and precipitation. These parameters are derived from ERA5 reanalysis data with a horizontal resolution of 0.25 degrees (https://cds.climate.copernicus.eu/cdsapp). The monthly temperature and salinity for model initialization are derived from the Ocean Reanalysis System 5 (ORAS5). The open boundary conditions are used to input daily temperature, salinity, and u- and v-velocity data, supporting the transport across the model's lateral boundaries. The barotropic velocity components of 10 significant tidal constituents in this region (namely, M_2, S_2, K_1, O_1, K_2, N_2, P_1, Q_1, M_4,and MS_4) are extracted from the TPXO

This article is protected by copyright. All rights reserved.

Author Manuscript

Author Manuscript

regional model for the Indian Ocean at 1/12° resolution (https://www.tpxo.net/regional) and used to force the model domain at the open boundaries The model integration started from the first day of each month and simulated for the entire month. The first 15 days are considered for the spin-up, allowing the model to reach equilibrium. This duration is sufficient for ITs to propagate throughout the model domain and aligns with previous studies (Mohanty et al., 2018; Tang et al., 2023; Xu et al., 2016; Yadidya et al., 2021, Yadidya et al. 2022a). Furthermore, the time series of domain-averaged sea surface height and kinetic energy confirm that the model attains equilibrium within this period (not shown here). Hence, the analysis is restricted to the last two weeks to account for the propagation of ITs throughout the model domain.

3 Results and Discussion

3.1 Analysis of IT using buoy data

In this section, we discuss the observational data from the buoy AD08, AD09, and AD10 for 2018, covering the entire year with only a few missing records in each. Figure 2 illustrates the rotary spectra analysis of the current vector at 100m, which is the typical pycnocline depth. The analysis separates the current vector into clockwise (CW) and counter-clockwise (CCW) rotating circular components with 30 degrees of freedom. At frequencies of near-inertial waves, the CW spectrum is found to be more dominant than the CCW spectrum, which aligns with the propagation pattern in the northern hemisphere. Usually, the inertial frequency (*f*) waves are generated by the action of surface winds and the frequency varies with latitude. In the present study, we restricted our analysis to tidal currents, even though near-inertial currents are important in the EAS. Our observations at the three-buoy locations indicate both diurnal and semidiurnal frequencies are the most dominant in the region. The constituents M_2, S_2, K_1, O_1, and *f* provide the most energy to the spectrum, and the energy peaks at diurnal and semidiurnal frequencies are about equal in magnitude. This is consistent with the study of Subeesh and Unnikrishnan (2016) on ADCP data collected over the shelf off the west coast of India. However, it is in contrast with that of the BoB (Mohanty et al., 2017) and the Andaman Sea (Yadidya et al., 2022a) where semidiurnal frequency dominates.

This article is protected by copyright. All rights reserved.

Author Manuscript

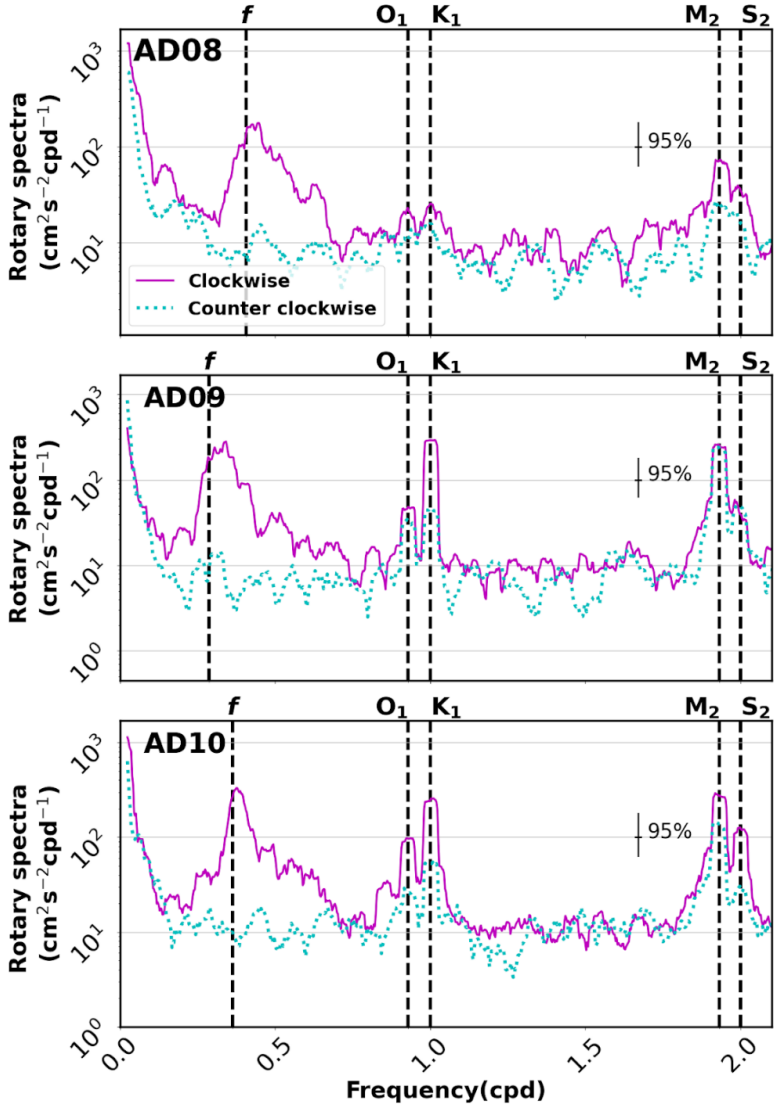

Figure 2. Rotary spectra of raw-current velocity at 100 m depth of AD08, AD09 and AD10 for 2018.

Further, barotropic and baroclinic ellipses (for varying depths) are computed through harmonic analysis to comprehend the barotropic and vertical structure of IT. Figure 3 shows tidal ellipses at all buoy locations, indicating that semidiurnal barotropic tides rotate CW and diurnal tides CCW. Figure 3 (e-h) also shows that baroclinic tidal currents rotate both CW and CCW at different depths across all buoy sites, regardless of frequency. The depth of the maximum baroclinic current (Table 1) suggests that M_2 and K_1 tidal components mainly dominate in this region followed by S_2 and O_1.

This article is protected by copyright. All rights reserved.

Author Manuscript

Table1. Maximum baroclinic current (MBC) and corresponding observed depth from the semi-major axis of M_2, S_2, K_1 and O_1.

Tidal constituents	**AD08**		**AD09**		**AD10**	
	MBC (cm/s)	**Depth** (m)	**MBC** (cm/s)	**Depth** (m)	**MBC** (cm/s)	**Depth** (m)
M_2	2.78	95	7.0	90	7.8	120
K_1	1.09	140	6.9	75	5.8	25
S_2	1.20	40	2.8	50	3.5	30
O_1	1.10	140	3.7	70	2.5	130

Higher eccentricity of the ellipse indicates stronger tidal currents flowing predominantly in specific directions, contrasting with the uniform tidal currents in all directions indicated by a circular tidal ellipse (Figure 3). Although the tidal ellipses also show some meridional effect, the ellipse mostly exhibits zonal flow. This could suggest generation at the shelf-slope break along the west coast of India and nearby islands. The spectral energy and baroclinic currents at AD08 are one order lower than those at AD09 and AD10. This could be explained by the fact that AD09 and AD10 are closer to the islands and shallower than AD08 (Figure 1).

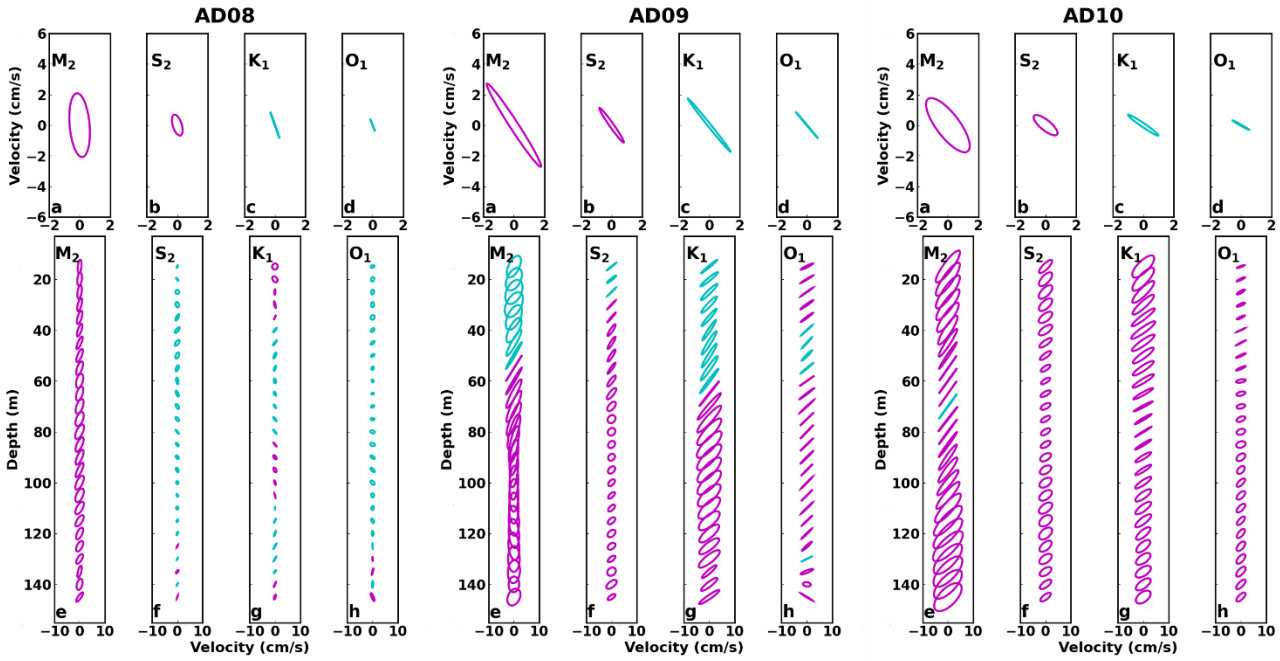

This article is protected by copyright. All rights reserved.

Author Manuscript

Figure 3. (a-d) Barotropic and (e-h) baroclinic tidal ellipses for the year 2018. Magenta colour represents the clockwise rotation, and blue colour represents counter-clockwise rotation

Using 2018 continuous density data at AD09, a Morlet wavelet transform technique (Büssow, 2007) with 95% cone of influence is used to examine time-frequency characteristics at 100m depth (Figure 4). The Morlet wavelet transform shows increased intensity at diurnal and semidiurnal tidal frequencies (Figure 4b). The intensity slowly increased from the end of January in the southeastern AS. This could be due to the weakening of northeast monsoon and increasing of solar radiation, which leads to higher stratification of the region. However, peak intensity is observed during the pre-monsoon months (April and May) when ocean surface warming strengthens ocean stratification. Furthermore, the atmospheric conditions during the pre-monsoon are comparatively calm and steady, which reduces surface mixing and permits increased IT activity (Longhurst, 2007). Strong winds create turbulence and a 100-120 m mixed layer during the monsoon season (Mathew et al., 2003). Turbulence lowers IT activity at this depth. The winds settle after the monsoon, and low-saline water from the BoB flows into the EAS across the Indian peninsula, increasing haline stratification at the surface. Furthermore, during the post-monsoon period (October and November), the thermal stratification deepens (Albert et al., 2023). Studies conducted as part of the Joint Global Ocean Flux Study have shown that the depth of the mixed layer in winter ranges from 80 to 120 meters (Sarma et al., 2019). Consequently, we observe the reduced intensity of IT at this depth.

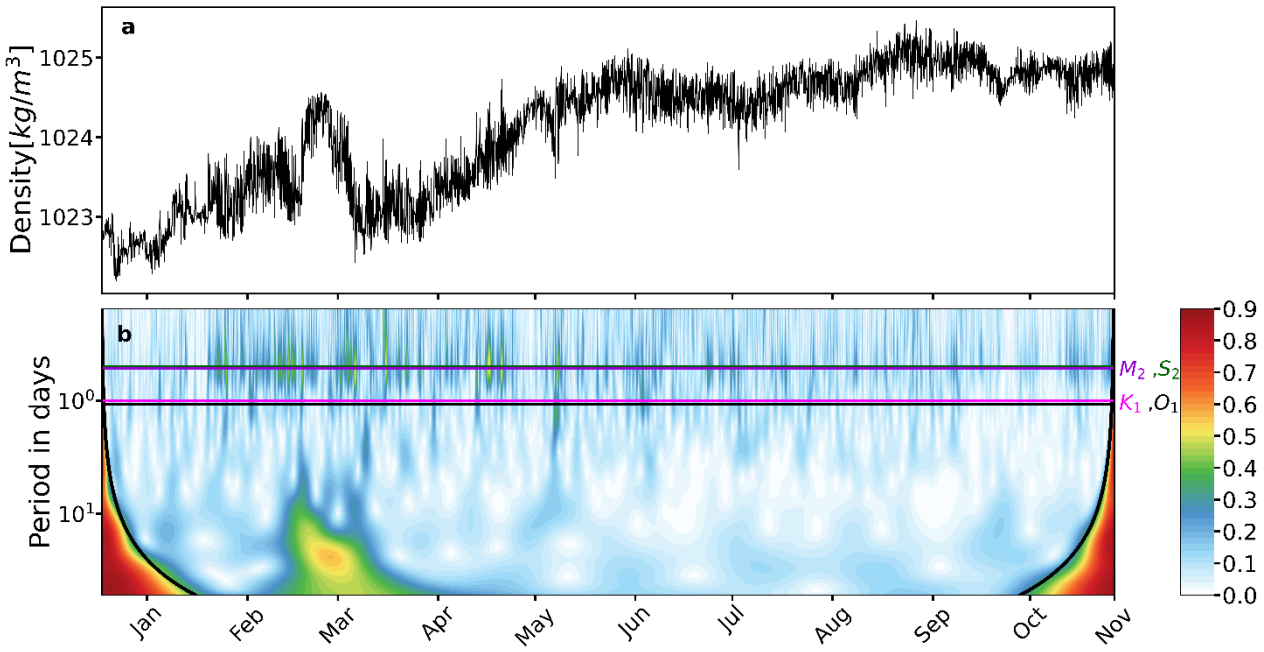

This article is protected by copyright. All rights reserved.

Author Manuscript

Figure 4. (a) Time series data of density of AD09 at 100m depth and (b) associated spectrum using Morlet wavelet transform method. The horizontal lines in (b) indicate the periodicity of each principal component.

3.2 Model Validation

We began by validating the MITgcm simulations against available observations of tides, circulation, and vertical profiles of temperature and salinity in Section 3.2. After validation, we used the model to simulate ITs and gain a better understanding of the governing mechanisms behind their generation, propagation, and dissipation. We also discuss the energy budget of ITs in regions where they are dominant.

3.2.1 Validation of tides

The validation of the barotropic tide involves comparison of the model's simulated sea surface elevation anomaly with tide-gauge data (Figure 5) at specific locations, viz., JNPT (Mumbai) (18.9ºN, 72.8ºE), Karwar (14.8ºN, 74.1ºE), Mangaluru (12.9ºN, 74.8ºE), and Kochi (9.9ºN, 76.3ºE). We chose the April 2018 data because tide-gauge information was available at all four locations. At JNPT (Mumbai), we observe a maximum root mean squared error (RMSE) of 0.18m. This occurs because JNPT is located inland from the coast (Figure 1). The higher RMSE could be due to the model's inability to fully capture the impact of the man-made port in Mumbai, along with the effects of local geographical features. The discrepancy in the model amplitudes noticed during the neap-tide may be attributed to the TPXO tidal data, in which the disagreement was also observed. However, the model effectively captures variations in sea surface elevation, exhibiting a strong correlation at all four stations (Figure 5). This indicates that the model accurately simulates tidal amplitude and its phase in the region of interest.

This article is protected by copyright. All rights reserved.

Author Manuscript

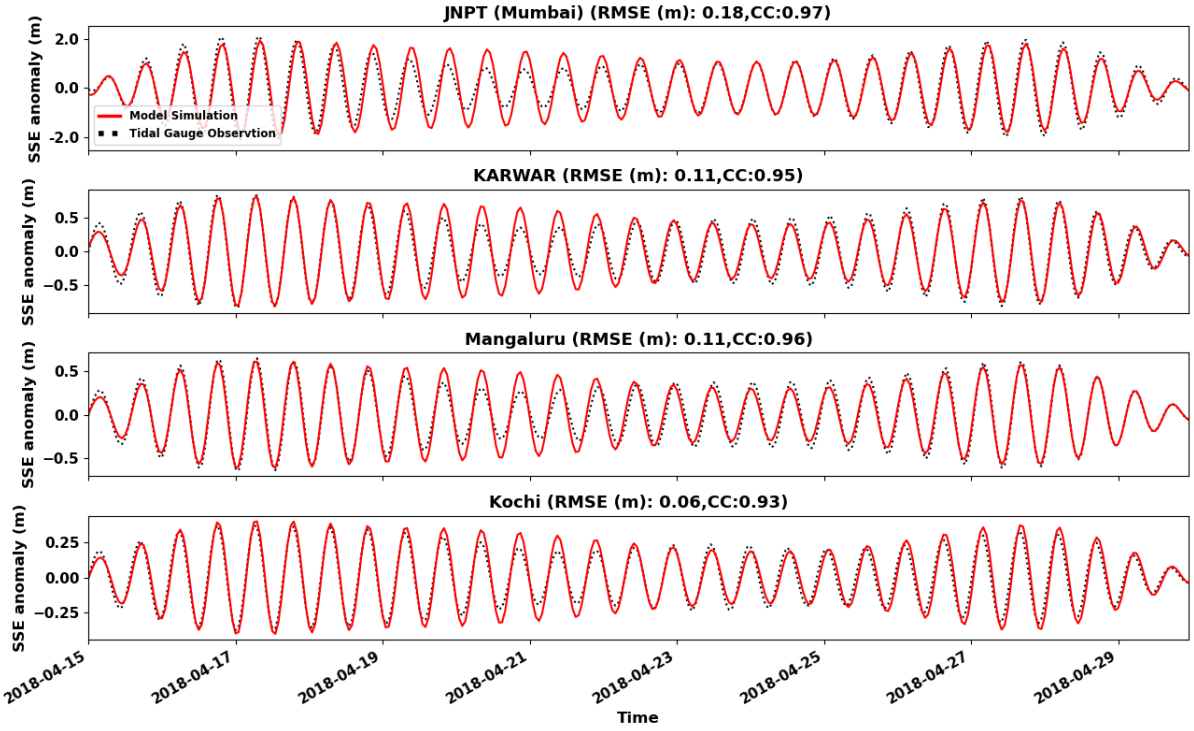

Figure 5. Comparison of model-simulated sea surface elevation anomaly with tide-gauge data at JNPT (Mumbai), Karwar, Mangaluru and Kochi for April 2018. The black dashed line represents tide-gauge observations, while the red solid line depicts the model simulations.

3.2.2 Validation of sea-surface circulation

The model simulated sea-surface circulation is authenticated using Ocean Surface Current Analysis (OSCAR) (http://www.oscar.noaa.gov /), which is available at every 0.25 degree and with a 5-day sampling resolution. The model utilizes both initial and boundary conditions from monthly climatology data spanning from 2000 to 2020. The OSCAR data is also used for the same period and computed monthly climatology for validation. The model simulation shown here only for representative summer monsoon of July and winter monsoon of January as depicted in Figure S1. These simulations highlight reversal of currents in these months as seen in the OSCAR data, which is mainly in response to seasonal reversal of monsoon winds. Moreover, an organized flow pattern during summer-monsoon and winter-monsoon is captured associated with Lakshadweep low/high, respectively as shown in the boxes. However, the Lakshadweep high is more prominent both in the observations and simulations compared to that of Lakshadweep low, which is also consistent with the earlier studies of Shetye (1998).

3.2.3 Validation of temperature and salinity

This article is protected by copyright. All rights reserved.

Author Manuscript

The model sea surface temperature is compared with the GHRSST (Group for High Resolution Sea Surface Temperature) MUR-JPL-L4-GLOB-v4.1 dataset, a Level-4 satellite-based analysis product with a 0.01° grid resolution, obtained from https://cmr.earthdata.nasa.gov/search. Similarly, the model's sea surface salinity is validated against the Multi Observation Global Ocean Sea Surface Salinity and Sea Surface Density (MULTIOBS_GLO_PHY_S_SURFACE_MYNRT_015_013) dataset, a daily global gap-free Level-4 analysis (0.125° resolution) produced using multivariate optimal interpolation of satellite observations, including SMAP and SMOS, combined with *in situ* measurements, derived from https://data.marine.copernicus.eu/. The model validation, both spatially and temporally, is presented for the summer monsoon (July) and winter monsoon (January), as illustrated in Figure S2. The calculated biases fall within the acceptable range across the entire domain.

As the simulations of vertical density profiles are important for the study of internal waves, temperature, and salinity profiles at the buoy locations of AD08, AD09, AD10 and RAMA are compared between the model and observations as shown in Figure S3. It is noted that temperature and salinity match reasonably well except at some depths, which may be attributed to the model initial conditions from the ORAS5. The RMSE of density, computed at each buoy location, ranges from 0.1 to 0.48 kg/m^3.

3.3 Energetics of IT

The spectral analysis of the density from buoy observations (AD08, AD09, AD10 and RAMA) and model simulations are carried out using fast Fourier transformation algorithm of Cooley and Turkey (1965). The periodic function is expressed as an infinite sum of periodic complex exponential functions such as

$$f(x) = a_0 + \sum_{n=1}^{\infty} a_n cos(n\pi x/L) + b_n sin(n\pi x/L)$$

where, a_0, a_n and b_n are Fourier constants. Figure 6 shows the comparison of the spectral estimates of density between observations and simulations. The comparison is made at 100m depth as the pycnocline depth at all the locations falls in the range of this depth. The model notably captures the dominant peaks of M_2, K_1, S_2 and O_1, which agrees with the observations. Our study focuses primarily on the semidiurnal and diurnal bands, where the model shows a good agreement. This is consistent with the rotary spectra of currents at 100m depth as shown in Figure 2.

This article is protected by copyright. All rights reserved.

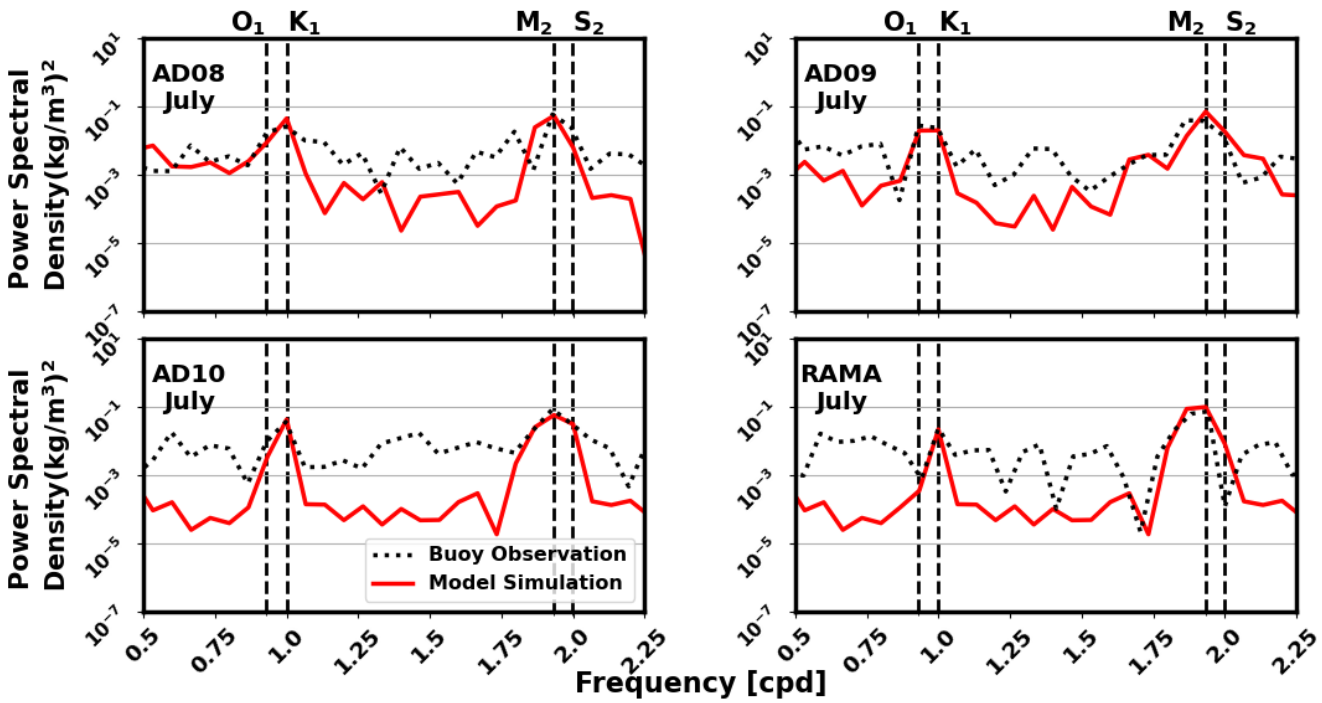

Figure 6. Comparison of spectral estimate of density at 100m depth. The solid line corresponds to buoy observations and the dashed line represents the model simulations

3.3.1 Generation sites of internal tides

As described in the methodology section, spatial pattern of the semidiurnal barotropic to baroclinic energy conversion rates integrated over the entire depth in the EAS during different seasons is computed. It is found that the sites are almost same for all the seasons as shown for April 2018 in Figure 7. A positive energy conversion rate indicates regions of IT generation.

It is observed that they are primarily generated along the shelf-slope along the coast. Our simulations suggest that the generation sites are primarily dominated in the three regions as marked by the boxes. In the top box denoted by SD1, generating sites are primarily confined along the continental shelf-slope of 130m off Mumbai coast. The other sites represented by SD2 and SD3 are in the regions of around Lakshadweep Islands and Maldives Islands respectively. The generation sites for diurnal ITs closely align with those of the semidiurnal tides (figure not shown).

This article is protected by copyright. All rights reserved.

Author Manuscript

Author Manuscript

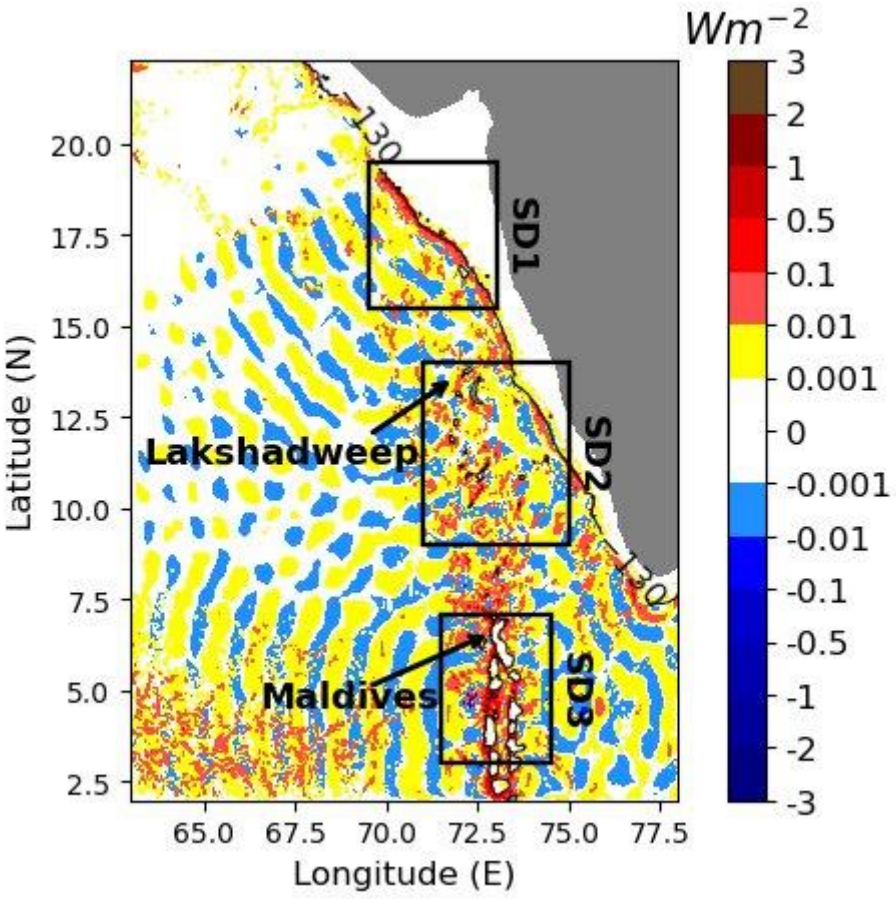

Figure 7. Depth-integrated semidiurnal barotropic-to-baroclinic energy conversion rate (Wm^{-2}) for April 2018. Bathymetry contour of 130 m is depicted. The boxes depict the sub-domains SD1, SD2 and SD3

The study of Ma et al. (2021) also indicated from the satellite observations that the M_2 semi-diurnal IT are mainly generated in the northeastern AS and Maldives Islands, which agrees with our simulations. We found that the maximum conversion rate is about 3 W/m^2 in the entire domain that is a little high compared to that of over the Western BoB, where the conversion rate is about 1 W/m^2 (Mohanty et al., 2017). The domain-integrated semidiurnal energy conversion rate from barotropic to baroclinic is approximately 11.77 GW, with about 66% (~ 7.79 GW) occurring on combining the Maldives and the northern shelf-slope region. Barotropic-to-baroclinic conversion rate depends on the phase difference between remotely generated IT and the local barotropic flow, compared to the cases in which the remotely generated IT are absent. The rate of energy conversion from barotropic to baroclinic modes is influenced by the phase relationship between internal tides generated remotely and the local barotropic flow. This rate can either increase or decrease based on this phase difference, relative to scenarios where no remotely generated internal tides are present (Mohanty et al., 2018).

This article is protected by copyright. All rights reserved.

Author Manuscript

These IT can also influence a portion of the converted energy that is locally dissipated (Kelly et al., 2012). The negative conversion rate indicates the energy transfer from the baroclinic tide to the barotropic tide (Mohanty et al., 2018). This is due to the difference in phase between the baroclinic tides generated locally and remotely as described by Zilberman et al. (2009). When integrated over the entire domain, the total positive conversion is approximately 28.41 GW, while the total negative conversion is -16.64 GW.

3.3.2 Variability of IT amplitudes

Amplitude of the IT is determined through computation of the isopycnal displacements for April 2018 which are estimated in accordance with Nash et al. (2005). The hovmöller diagram of isopycnal displacements for each sub-domain at a depth of 130 m is shown in Figure 8 as the shelf-break depth along the entire west coast of India is seen at about 130 m (Poulose et al., 2018). The computations are made using averaged over the latitudes of each sub-domain. The maximum amplitude of IT of about 23 m is observed in SD1 and mostly propagating away from the shelf region. However, its magnitude gradually decreases as they move away from the source of origin. Similarly, the maximum magnitude of IT in SD2 is noticed about 19 m close to the shelf region and propagating westwards. While in SD3, the maximum amplitude is about 15 m and propagating either side of the Maldives islands. From these simulations, the northern part of EAS shows higher IT amplitudes compared to that of other regions. This can be attributed due to the high tidal elevation of 1.2m over the shelf region in SD1, which slowly reduces towards south to about 0.5m in SD3 as observed in the tide data from both TPXO9 data and model. The computed isopycnal displacements over this region of EAS resembles to that of western BoB (Mohanty et al., 2017).

This article is protected by copyright. All rights reserved.

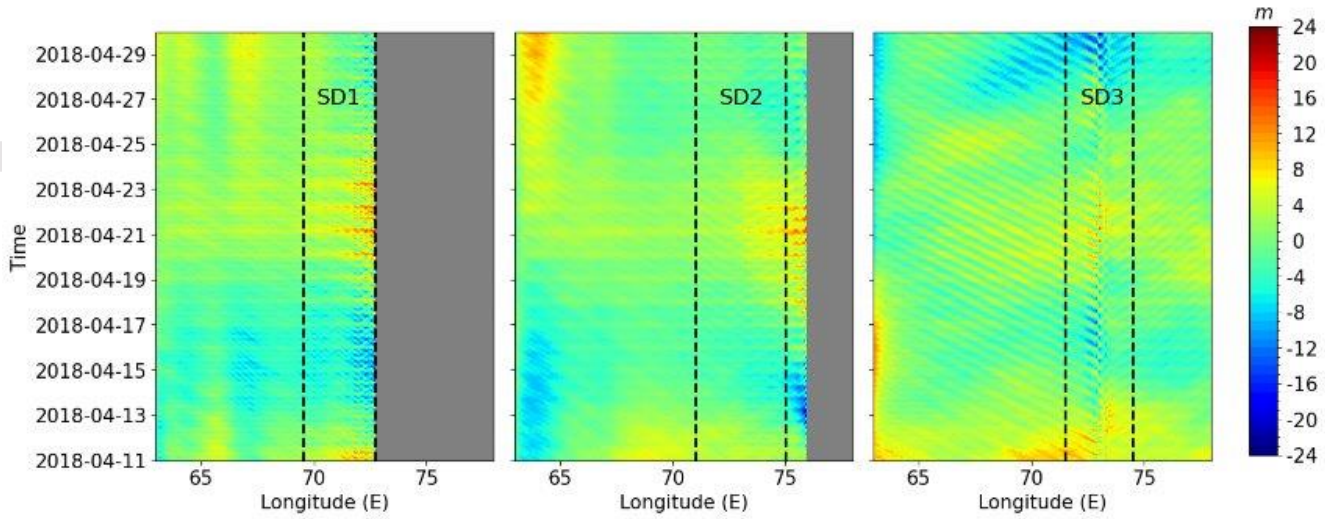

Figure 8. Hovmöller diagram of isopycnal displacements averaged over the latitudes of sub-domains SD1, SD2 and SD3 at 130 m depth for April 2018.

3.3.3 Seasonal energy density of IT

Energy density is defined as the sum of Available Potential Energy (APE) and Horizontal Kinetic Energy (HKE). The depth-integrated APE acts as the primary force for IT activity, which enhances the displacement of water masses within the interior of the ocean. It functions as a storage of energy that is contained in the differences of density within the water column, which is crucial for maintaining dynamic internal wave phenomena. A portion of the potential energy is transformed into kinetic energy, which ultimately aids in the process of mixing. Figure 9(a-d) illustrates the depth-integrated baroclinic semidiurnal APE, Figure 9(e-h) shows their corresponding HKE and Figure 9(i-l) represents the corresponding energy density. The months of January, April, July, and October, representing winter, pre-monsoon, monsoon, and post-monsoon respectively, are considered to study the seasonal variability.

It can be seen from Figure 9 that the energy density is pronounced mostly at the generation sites. The western part of the Maldives archipelago (SD3) is noted to have the highest APE and HKE during the summer monsoon. This indicates a possibility of wave superposition and local dissipation, both of which may have contributed to the enhanced propagation towards the western side and, ultimately, to mixing. The northern side of SD3 has a greater HKE, indicating the occurrence of mixing around SD2 region. During the post-monsoon, we notice that the APE exhibits a different spatial pattern to that of summer as it is seen in the north of SD3 instead of west. During the pre-monsoon season (April), both APE and HKE in the SD1 region are higher compared to other seasons. This suggests that the SD1 region may experience more intense IT

This article is protected by copyright. All rights reserved.

Author Manuscript

Author Manuscript

activity during this period. The peak APE and HKE values are relatively low in winter compared to other seasons. In the Gulf of Khambat, some amount of APE is also noticed in July and October due to presence of more stratified waters as reported in the study of Rao et al. (2009). The Richardson number (Ri) is a key indicator of turbulent mixing caused by density overturning and velocity shear. The instability occurs when Ri drops below 0.25, and the flow remaining stable only when Ri is 0.25 or higher. Figure S4 shows the Ri values at the locations off Mumbai (19.07ºN), Kochi (9.93ºN) and Male (4.17ºN) in the respective sub-domains of SD1, SD2, and SD3 during the spring tide on 28th July 2018. Low values of Ri indicate that mixing might be more pronounced in the continental shelf-slope region and around the islands.

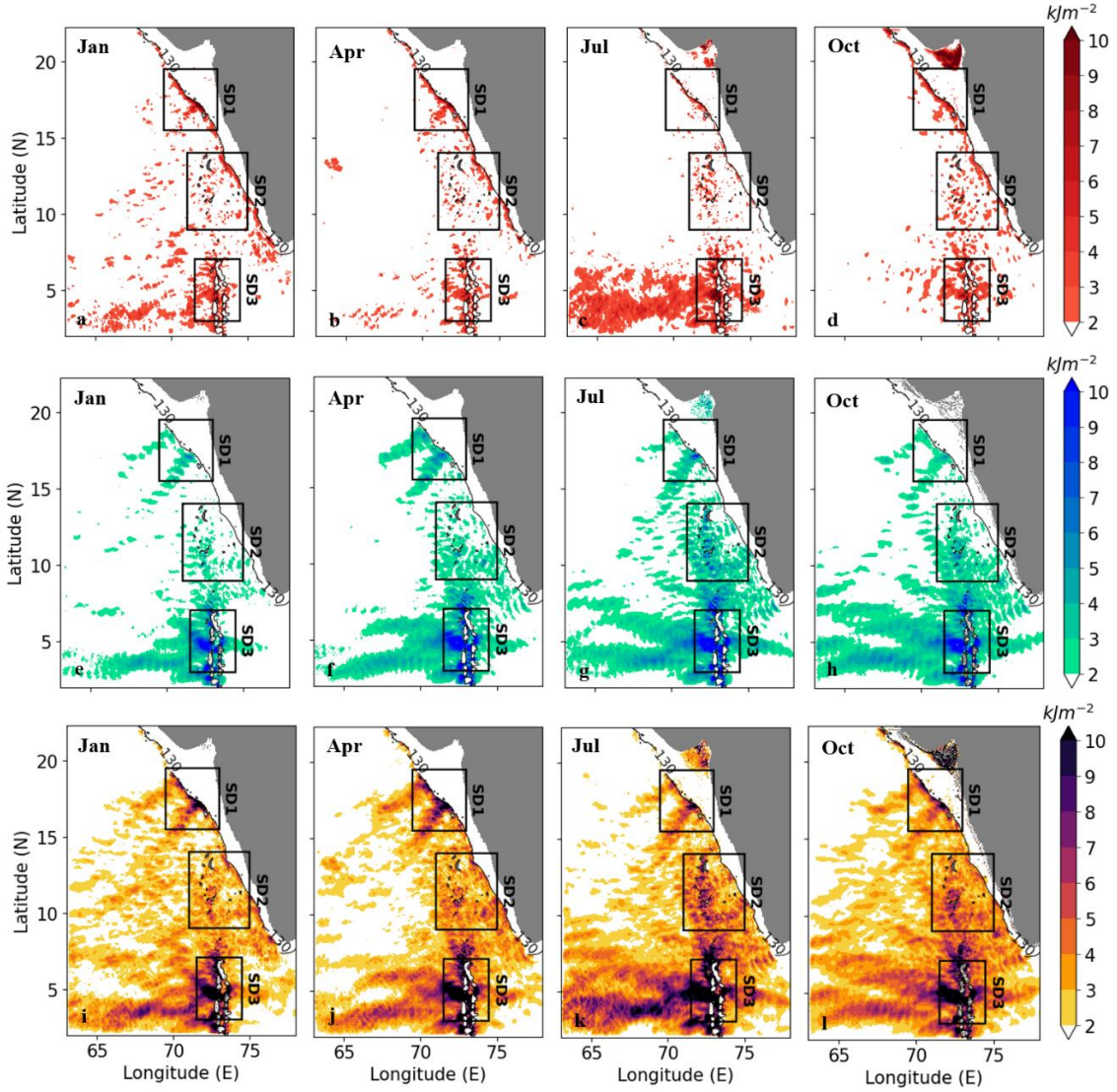

Figure 9. (a-d) Depth-integrated baroclinic semidiurnal APE, (e-h) HKE, (i-l) APE+HKE for January, April, July, and October of 2018. Bathymetry contour of 130 m is depicted

This article is protected by copyright. All rights reserved.

Author Manuscript

3.3.4 Seasonal propagation of internal tides

When the barotropic tides in the EAS move northeastward and reach the point where the continental shelf drops off, they create a disturbance due to the change in topography. This disturbance then transforms into waves of varying intensities, which primarily propagate away from the shore. The spatial pattern of depth-integrated energy flux for semidiurnal frequency is shown in Figure 10 for seasonal representative months of January, April, July, and October. In general, it is observed in all the months that the propagation is outwards from the sites of generation. In the northern continental shelf-slope region of SD1, the IT propagation exhibits two primary branches: one that moves in a southwesterly direction towards the central AS, and another that

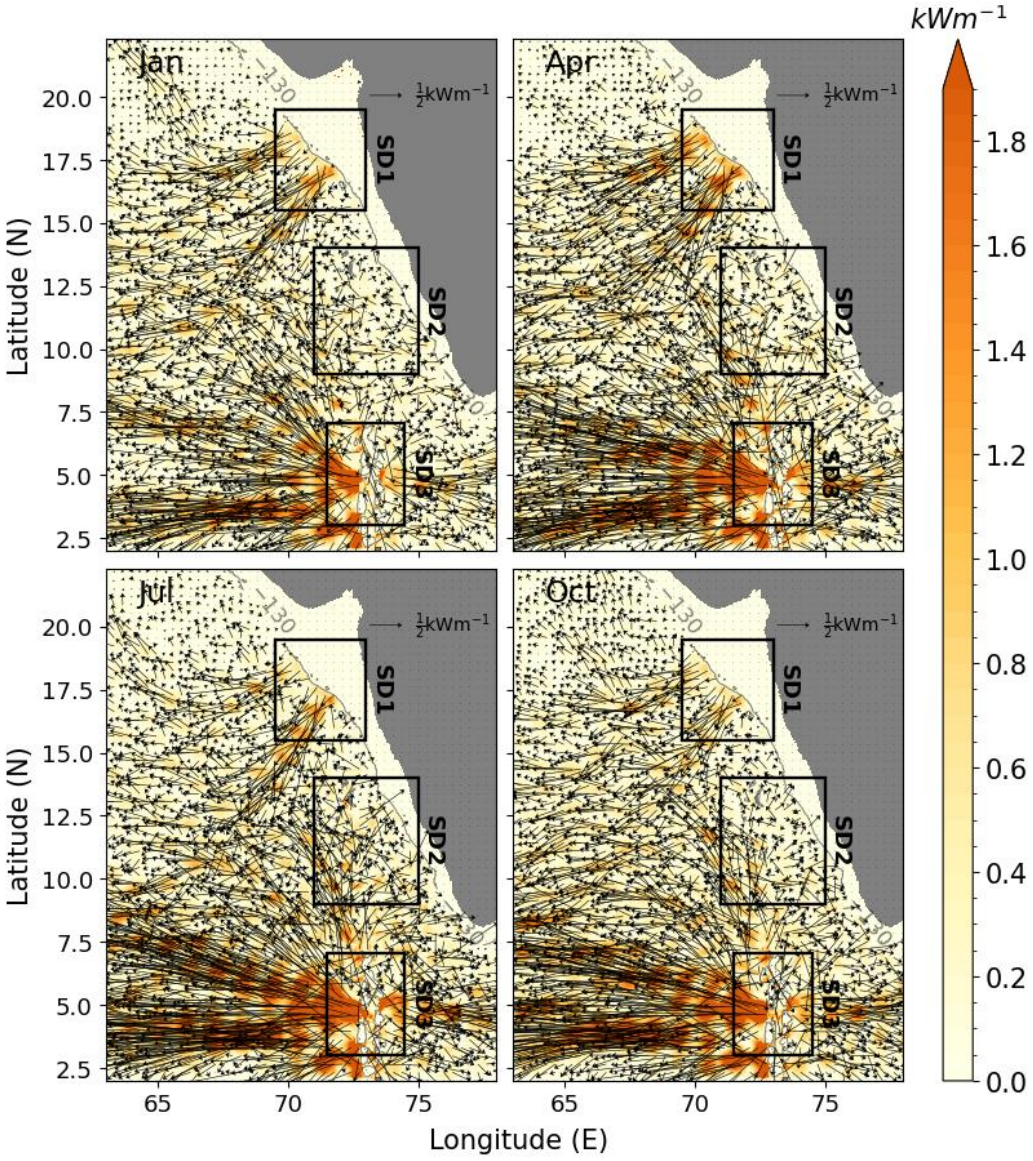

This article is protected by copyright. All rights reserved.

Author Manuscript

Figure 10. Semidiurnal baroclinic energy flux (vectors are plotted for every seven grid points in each direction) for January, April, July and October of 2018. Bathymetry contour of 130m is depicted.

moves westward with more inclination to the south. This may be attributed to the prevailing high tides and complex coastal geometry of this region. However, this requires further investigation, which is beyond the scope of the present study. From the most potent generation site of SD3, a significant portion of the energy moves westward, as it may be influenced by the presence of westward propagating Rossby waves. Amol et al. (2020) reported that the signatures of Rossby waves are clearly visible in satellite ocean color data in the EAS, showing a westward drift. Additionally, they noted that meridional advection is stronger in the northwest region near the Maldives. Also, in our model simulations some parts of the energy are also seen propagating towards the east, and very little energy is propagating toward the north and south. The region of Lakshadweep islands represented by SD2 is mainly influenced by the propagating waves from SD1 and SD3, resulting in superposition of waves with no clear direction.

Our study in these regions is consistent with the study of Ma et al. (2021), which detects similar propagation characteristics of M_2 ITs using various satellite data. The computed peak energy fluxes at the boundaries of SD1 are 1.15, 1.40, 0.86, and 0.84 kWm^{-1}, while for SD3, they are 3.44, 4.29, 5.27, and 5.03 kWm^{-1} for January, April, July, and October, respectively. This infers that the propagation is intense in April followed by January for SD1, while it is July and October for SD3. Compared to SD1, the peak energy fluxes are noticed in the SD3, which is aligning with our previous assertion that the presence of isolated Maldives islands leads to increased generation of IT in the SD3 region (refer Figure 7), resulting in more propagation across all seasons. In the SD2 subdomain, although the energy flux does not have a well-defined propagation direction, the peak value is observed in July at 1.08 kWm^{-1}, followed by 1.03 kWm^{-1} in October at the boundaries. For a better visualization of IT propagation in the region, hourly vertical velocity at 130m depth for a period of 20 days in April 2018, covering the complete tidal cycle, is depicted in Movie S1.

3.3.5 Seasonal variability of energy budget

The baroclinic tidal energy budget associated with semidiurnal and diurnal is computed in each sub-domain for different months as depicted in Figure 11. On the sub-domain boundaries, the depth-integrated and area-integrated barotropic to baroclinic energy conversion is denoted by

This article is protected by copyright. All rights reserved.

orange; baroclinic dissipation by blue and the depth-integrated baroclinic energy flux by magenta numbers. The negative value represents the westward or southward direction of the energy flux.

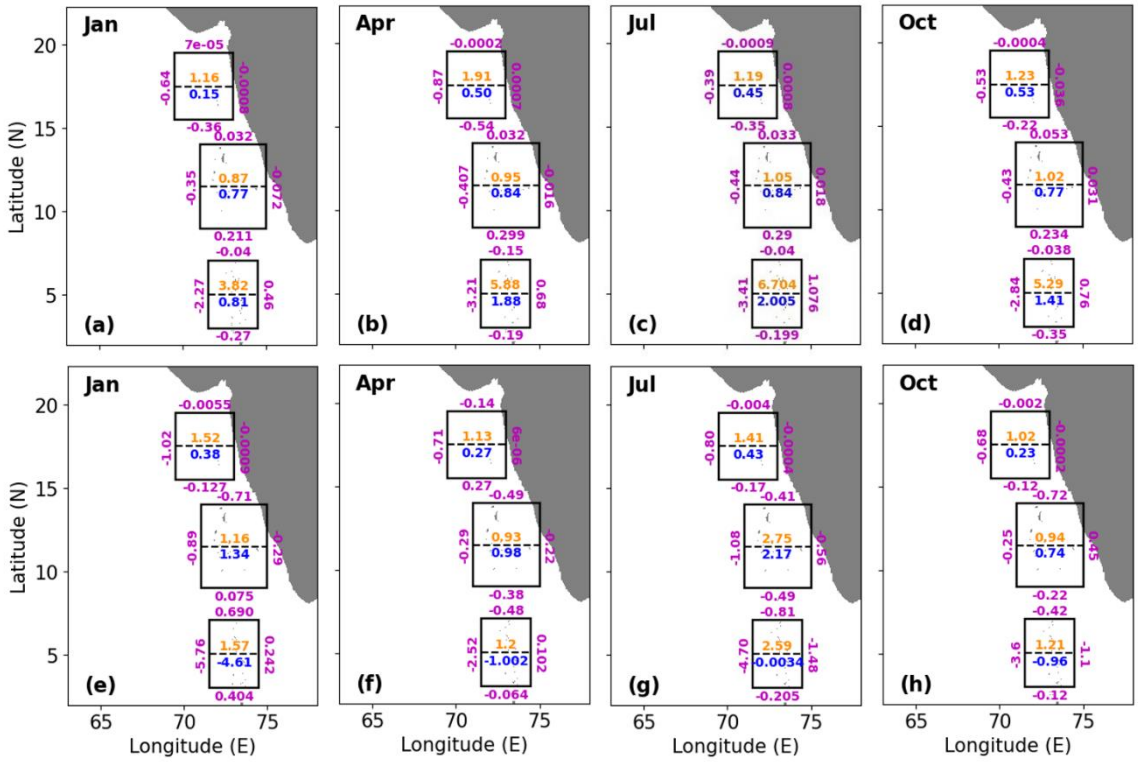

Figure 11. Seasonal comparison of baroclinic tidal energy budget for frequencies of (a-d) semidiurnal, (e-h) diurnal.

For any season in SD1, semidiurnal fluxes are observed large in the western and southern boundaries compared to other two boundaries (Figure 11 a-d), inferring that most of the energy is propagating westward and/or southward. The energy conversion in SD1 exhibits its peak of about 1.91 GW with a local dissipation of about 0.50 GW during the pre-monsoon month of April, advocating that about 26% of its energy is locally dissipated. The conversion of energy is more in October after April with about 43% of local dissipation. Although energy conversion is nearly the same in January (1.16 GW) and July (1.19 GW), the dissipation in January is only about 13%, indicating that the associated energy fluxes are higher during this month. Further, a relatively low-energy conversion is noted in SD2 ranging from 0.87 to 1.05 GW, with large local dissipation between 75% and 88% across different seasons. While for SD3 region, the energy conversion is higher in all the months compared to the other two sub-domains. A

This article is protected by copyright. All rights reserved.

Author Manuscript

maximum of about 6.7 GW in July and a minimum of 3.82 GW in January is observed.Seasonal variability is more pronounced in the SD3 region for the semidiurnal frequency, with a standard deviation of 1.03 GW.

The diurnal energy conversion (Figure 11 e-h) in the SD1 and SD2 region is comparable to that of the semidiurnal. In SD1, the energy conversion is seen maximum in January/ July , while it is in April for semidiurnal. However, the dissipation at diurnal frequency ranges between approximately 22 - 30% over the four months in SD1. The diurnal energy fluxes observed at the sub-domain boundaries display a similar pattern to the semidiurnal fluxes, with the highest values occurring mainly along the western and southern boundaries, particularly in the northern region. The SD2 region demonstrates its highest diurnal energy conversion during July, ranging from 0.93 to 2.75 GW across all seasons following almost similar patterns as seen in the case of semidiurnal. In January and April, the notably higher dissipation compared to energy conversion suggests the influence of remotely dissipated energy transmitted from other generation sites (Peng et al., 2021). In SD2, both semidiurnal and diurnal energy conversion rates are nearly identical, which aligns with our observational analysis using AD09 and AD10 time series data, as these two buoys are in close proximity to this domain (refer section 3.1 and Figure 2). The model simulations in SD2 also agree with the study of Subeesh et al. (2013), where diurnal K_1 is observed significantly on the shelf off Kollam at around 9°N using the ADCP current data. The energy conversion in the SD3 varies between 1.2 and 2.59 GW with its peak value in July. The diurnal energy conversion is comparatively lower than the semidiurnal energy conversion, ranging between 23-41% across all the months. Nevertheless, it consistently demonstrates higher energy conversion rates compared to other sub-domains across multiple months. The diurnal energy fluxes are observed to be similar to semidiurnal where the westward flow seems dominant for all the months. Diurnal energy conversion varies seasonally from 0.20 to 0.76 GW, with the highest variability observed mainly in the southern region.

4 Conclusions

Temporal variability of IT is comprehensively documented using moored buoy data available at different locations spread over the EAS for 2018. The internal wave spectrum is predominantly characterized by inertial, diurnal, and semidiurnal frequencies, in contrast to the BoB region, where the energy associated with diurnal frequency is not readily discernible. The analysis from the observations indicates that the M_2 and K_1 tidal components are the most

This article is protected by copyright. All rights reserved.

Author Manuscript

Author Manuscript

leading in this region, followed by S_2 and O_1. Comparing spectral energy and baroclinic currents across all buoy locations shows that the highest values occur at buoys positioned in shallower regions and near the islands.

The MITgcm is used in this study to simulate IT by forcing the model with 10 major tidal constituents. The simulations are delineated to understand the seasonal variability of IT generation, propagation, and dissipation in the EAS. The stratification varies seasonally as well as region wise with increasing stratification from north to south. The simulated spectral estimate of density in the pycnocline depth indicates that the peak estimate is associated with both diurnal and semidiurnal frequencies with a comparable magnitude, which agrees from the observations. The positive barotropic to baroclinic energy conversion observed in the northern shelf-slope region, Lakshadweep islands, and Maldives islands indicates that these zones are the prominent for generation of IT. The amplitude of IT reaches the maximum of 23m in northern EAS around Mumbai, while it is only 19m and 15m in Lakshadweep and Maldives respectively. The amplitude gradually lessens offshore from the generation sites. Despite low amplitudes of the tide of about 1m in Maldives islands, a substantial conversion of barotropic to baroclinic energy is noted. This may be because of several islands that are close together, creating multiple generation sites. The IT propagation is observed predominantly southwestward from shelf break region off Mumbai and westward from Maldives. Propagation in Lakshadweep is mainly influenced by waves from both the northern shelf break region and the Maldives, resulting in the interference of waves.

An attempt is also made, for the first time, to study the seasonal variability IT in the EAS using the model. From the budget analysis, it is observed that higher semidiurnal energy conversion is found in April for northern EAS and in July for southern EAS around Maldives. Hence, the semidiurnal energy flux follows the same pattern as the barotropic-to-baroclinic energy conversion, peaking in April off Mumbai and in July near the Lakshadweep and Maldives. Compared to along the continental shelf-slope near Mumbai and Lakshadweep, the energy conversion and energy fluxes are spotted higher in the Maldives in all the months. Upon comparing the simulations, it is observed that higher energy fluxes are associated with lesser baroclinic dissipation. High energy conversion at the diurnal frequency is observed in January and July near the continental shelf-slope off Mumbai and in July near Lakshadweep and the Maldives. From the energy fluxes, it is noted that diurnal frequency propagation in any season is predominantly southwestward for the continental shelf-slope near Mumbai, mirroring the pattern observed for semidiurnal frequency. Similarly, Maldives exhibits westward energy flux

This article is protected by copyright. All rights reserved.

Author Manuscript

propagation, also akin to semidiurnal patterns. It is also noticed in Maldives that the energy conversion and associated fluxes are higher for semidiurnal compared to diurnal, while it is almost the same along the continental shelf-slope near Mumbai and Lakshadweep. The study helps in outlining the IT characteristics, generation sites and its energy budget associated with semidiurnal and diurnal frequencies in the EAS.

Author Contributions

P. Makar: Conceptualization, Formal analysis, Investigation, Methodology, Software, Validation, Visualization, Writing – original draft, Writing – review & editing. **A. D. Rao:** Conceptualization, Investigation, Methodology, Supervision, Visualization, Writing – review & editing. **B Yadidya:** Methodology, Software, Writing – review & editing. **Vimlesh Pant:** Writing – review & editing.

Acknowledgements

The authors are thankful to the Naval Research Board (NRB), Government of India, for the financial support for carrying out this study. The authors are also thankful to the National Institute of Ocean Technology, Chennai, for providing *in-situ* buoy observation data, the Indian National Centre for Ocean Information Services for providing tide-gauge data. The authors also thank the Indian Institute of Technology Delhi HPC (High Performance Computing) facility for affording computational resources. The first author acknowledges PMRF fellowship for financial support in the form of her research fellowship.

Data Availability Statement

RAMA buoy data can be downloaded from https://www.pmel.noaa.gov/tao/drupal/disdel/. Tide gauge data, as well as buoy data for AD08, AD09, and AD10, is available from (Pragnya, 2025). The internal tide energy budget and the post-processing of model simulations were calculated using Xmitgcm (Abernathey et al., 2021) and xgcm (Abernathey et al., 2022).

References

Abernathey, R., Dussin, R., Smith, T., Fenty, I., Bourgault, P., Jones, S., et al. (2021). MITgcm/xmitgcm: v0.5.2 (Version v0.5.2) [Computer software]. Zenodo. https://doi.org/10.5281/ZENODO.5139886

This article is protected by copyright. All rights reserved.

Author Manuscript

Abernathey, R., Busecke, J., Smith, T., Jdldeauna, Banihirwe, A., Nicholas, T., et al. (2022). xgcm/xgcm: v0.6.2rc1 (Version v0.6.2rc1) [Computer software]. Zenodo. https://doi.org/10.5281/ZENODO.6097129

Albert, J., Gulakaram, V. S., Vissa, N. K., Bhaskaran, P. K., & Dash, M. K. (2023). Recent warming trends in the Arabian Sea: Causative factors and physical mechanisms. *Climate*, 11(2), 35. https://doi.org/10.3390/cli11020035

Amol, P., Bemal, S., Shankar, D., Jain, V., Thushara, V., Vijith, V., & Vinayachandran, P. N. (2020). Modulation of chlorophyll concentration by downwelling Rossby waves during the winter monsoon in the southeastern Arabian Sea. Progress in Oceanography, 186, 102365. https://doi.org/10.1016/j.pocean.2020.102365

Buijsman, M. C., Uchiyama, Y., McWilliams, J. C., & Hill-Lindsay, C. R. (2012). Modeling semidiurnal internal tide variability in the Southern California Bight. *Journal of Physical Oceanography*, 42(1), 62-77. https://doi.org/10.1175/2011JPO4597.1

Büssow, R. (2007). An algorithm for the continuous Morlet wavelet transform. *Mechanical Systems and Signal Processing*, 21(8), 2970-2979. https://doi.org/10.1016/j.ymssp.2007.06.001

Chuang, W.-S., & Wang, D.-P. (1981). Effects of density front on the generation and propagation of internal tides. *Journal of Physical Oceanography, 11*(10), 1357–1374. https://doi.org/10.1175/1520-0485(1981)011<1357:EODFOT>2.0.CO;2

Cooley, J. W., & Tukey, J. W. (1965). An algorithm for the machine calculation of complex Fourier series. *Mathematics of Computation*, 19(90), 297–301. https://doi.org/10.2307/2003354

Egbert, G. D., & Erofeeva, S. Y. (2002). Efficient inverse modeling of barotropic ocean tides. Journal of Atmospheric and Oceanic Technology, 19(2), 183–204. https://doi.org/10.1175/1520-0426(2002)019<0183:EIMOBO>2.0.CO;2

Egbert, G. D., & Ray, R. D. (2000). Significant dissipation of tidal energy in the deep ocean inferred from satellite altimeter data. *Nature*, 405, 775–778. https://doi.org/10.1038/35015531

Gangadhara Rao, L. V., & Shreeram, P. (2005). Upper ocean physical processes in the Tropical Indian Ocean: A monograph prepared under CSIR Emeritus Scientist Scheme. National Institute of Oceanography, Regional Centre, Visakhapatnam, Andhra Pradesh, India. Retrieved from http://drs.nio.org/drs/bitstream/2264/93/1/UOPP.pdf

Garrett, C., & Kunze, E. (2007). Internal Tide Generation in the Deep Ocean. *Annual Review of Fluid Mechanics*, 39(1), 57–87. https://doi.org/10.1146/annurev.fluid.39.050905.110227

Hareesh Kumar, P. V., Lekshmi, S., Jagadeesh, P. S. V., Anilkumar, K., Krishnakumar, G. V., & Rao, A. D. (2010). Internal tides in the coastal waters of NE Arabian Sea: Observations and simulations. *Marine Geodesy*, 33(2–3), 232–244. https://doi.org/10.1080/01490419.2010.493494

Joseph, K. A., Jayaram, C., Nair, A., George, M. S., Balchand, A. N., & Pettersson, L. H. (2019). Remote sensing of upwelling in the Arabian Sea and adjacent near-coastal regions. In V. Barale & M. Gade (Eds.), *Remote sensing of the Asian seas* (pp. 563-574). Springer. https://doi.org/10.1007/978-3-319-94067-0_26

This article is protected by copyright. All rights reserved.

Author Manuscript

Kaur, H., & Buijsman, M. (2022). Seasonal variability of global internal tides. *Ocean Sciences Meeting 2022*. https://doi.org/10.24400/527896/a03-2022.3324

Kelly, S. M., Nash, J. D., Martini, K. I., Alford, M. H., & Kunze, E. (2012). The cascade of tidal energy from low to high modes on a continental slope. Journal of Physical Oceanography, 42(7), 1217–1232. https://doi.org/10.1175/JPO-D-11-0231.1

Kunze, E., Rosenfeld, L. K., Carter, G. S., & Gregg, M. C. (2002). Internal waves in Monterey Submarine Canyon. *Journal of Physical Oceanography*, 32, 1890–1913. https://doi.org/10.1175/1520-0485(2002)032<1890:IWIMSC>2.0.CO;2

Large, W. G., McWilliams, J. C., & Doney, S. C. (1994). Oceanic vertical mixing: A review and a model with a nonlocal boundary layer parameterization. *Reviews of Geophysics*, 32(4), 363-403. https://doi.org/10.1029/94RG01872

Longhurst, A. R. (2007). The Indian Ocean. In A. R. Longhurst (Ed.), *Ecological Geography of the Sea* (2nd ed., pp. 275-325). Academic Press. https://doi.org/10.1016/B978-012455521-1/50011-5

Ma, J., Guo, D., Zhan, P., & Hoteit, I. (2021). Seasonal M_2 internal tides in the Arabian Sea. *Remote Sensing*, 13(14), 2823. https://doi.org/10.3390/rs13142823

Ma, J., Guo, D., Zhan, P., & Hoteit, I. (2023). Variability and energy budget of the baroclinic tides in the Arabian Sea. *Frontiers in Marine Science*, 10, Article 1293814. https://doi.org/10.3389/fmars.2023.1293814

Mathew, B., Hareesh Kumar, P. V., & Rao, R. R. (2003). Mixed layer variability at selected locations in the Arabian Sea during pre and summer monsoon seasons: Observations and simulations. *MAUSAM*, *54*(4), 917-928

Marshall, J., Adcroft, A., Hill, C., Perelman, L., & Heisey, C. (1997). A finite-volume, incompressible Navier Stokes model for studies of the ocean on parallel computers. *Journal of Geophysical Research*, 102(C3), 5753–5766. https://doi.org/10.1029/96JC02775

McPhaden, M. J., Meyers, G., Ando, K., Masumoto, Y., Murty, V. S. N., Ravichandran, M., et al. (2009). RAMA: The research moored array for African–Asian–Australian monsoon analysis and prediction. *Bulletin of the American Meteorological Society*, 90(4), 459–480. https://doi.org/10.1175/2008BAMS2608.1

Mohanty, S., Rao, A. D., & Latha, G. (2018). Energetics of semidiurnal internal tides in the Andaman Sea. *Journal of Geophysical Research: Oceans*, 123(9), 6224-6240. https://doi.org/10.1029/2018JC013852

Mohanty, S., Rao, A. D., & Pradhan, H. K. (2017). Estimates of internal tide energetics in the western Bay of Bengal. *IEEE Journal of Oceanic Engineering*. Advance online publication. https://doi.org/10.1109/JOE.2017.2765978

Mohanty, S., Rao, A. D., & Yadidya, B. (2019). Spatial and temporal variability of semidiurnal internal tide energetics in the western Bay of Bengal. Pure and Applied Geophysics, 176(12), 5203–5215. https://doi.org/10.1007/s00024-019-02221-4

This article is protected by copyright. All rights reserved.

Author Manuscript

Munk, W., & Wunsch, C. (1998). Abyssal recipes II: Energetics of tidal and wind mixing. *Deep Sea Research Part I: Oceanographic Research Papers*, 45, 1977-2010. https://doi.org/10.1016/S0967-0637(98)00070-3

Nash, J. D., Alford, M. H., & Kunze, E. (2005). Estimating internal wave energy fluxes in the ocean. *Journal of Atmospheric and Oceanic Technology*, 22(10), 1551–1570. https://doi.org/10.1175/JTECH1784.1

Peng, S., Liao, J., Wang, X., Liu, Z., Liu, Y., Zhu, Y., ... et al. (2021). Energetics-based estimation of the diapycnal mixing induced by internal tides in the Andaman Sea. *Journal of Geophysical Research: Oceans*, 126(4). https://doi.org/10.1029/2020JC016521

Poulose, J., Rao, A. D., & Bhaskaran, P. K. (2018). Role of continental shelf on non-linear interaction of storm surges, tides and wind waves: An idealized study representing the west coast of India. *Estuarine, Coastal and Shelf Science*, 207, 457-470. https://doi.org/10.1016/j.ecss.2017.06.007

Pradhan, H. K., Rao, A. D., Reddy, K. K. G., & Mohanty, S. (2014). Internal wave simulation for different angles and shapes of continental shelf. In *2014 Oceans - St. John's*. St. John's, NL, Canada: IEEE. https://doi.org/10.1109/OCEANS.2014.7003050

Pradhan, H. K., Rao, A. D., & Mohanty, S. (2016). Inter-seasonal variability of internal tides in the western Bay of Bengal. *Natural Hazards*, 84(2), 809–820. https://doi.org/10.1007/s11069-016-2459-x

Pragnya, P. M. (2025). Data used for studying the seasonal variability of internal tides in the Eastern Arabian Sea (Version 1). Mendeley Data. https://doi.org/10.17632/fgy2b78k4f.1

Rao, A. D., Babu, S. V., Prasad, K. V. S. R., Ramana Murty, T. V., Sadhuram, Y., & Mahapatra, D. K. (2010). Investigation of the generation and propagation of low frequency internal waves: A case study for the East coast of India. *Estuarine, Coastal and Shelf Science*, 88(1), 143-152. https://doi.org/10.1016/j.ecss.2010.03.010

Rao, A. D., Joshi, M., & Ravichandran, M. (2009). Observed low-salinity plume off Gulf of Khambhat, India, during post-monsoon period. *Geophysical Research Letters*, 36, Article L03605. https://doi.org/10.1029/2008GL036091

Rao, R. R., & Sivakumar, R. (1999). On the possible mechanisms of the evolution of a mini-warm pool during the pre-summer monsoon season and the genesis of onset vortex in the southeastern Arabian Sea. *Quarterly Journal of the Royal Meteorological Society*, 125(555), 787–809. https://doi.org/10.1002/qj.49712555503

Sarma, V. V. S. S., Patil, J. S., Shankar, D., & Anil, A. C. (2019). Shallow convective mixing promotes massive Noctiluca scintillans bloom in the northeastern Arabian Sea. *Marine Pollution Bulletin, 138*, 428-436. https://doi.org/10.1016/j.marpolbul.2018.11.054

Sharples, J., & Zeldis, J. R. (2019). Variability of internal tide energy, mixing, and nitrate fluxes in response to changes in stratification on the northeast New Zealand continental shelf. New Zealand Journal of Marine and Freshwater Research, 54(1), 94–111. https://doi.org/10.1080/00288330.2019.1705357

Shetye, S. R., Gouveia, A. D., Shenoi, S. S. C., Michael, G. S., Sundar, D., Almedia, A. M., & Santanam, K. (1991). The coastal current off western India during the northeast monsoon. Deep

This article is protected by copyright. All rights reserved.

Author Manuscript

Sea Research Part A. *Oceanographic Research Papers*, 38(12), 1517-1529. https://doi.org/10.1016/0198-0149(91)90087-V

Shetye, S. R. (1998). West India Coastal Current and Lakshadweep High/Low. *Sadhana*, 23, 637–651. https://doi.org/10.1007/BF02744586

Smagorinsky, J. (1963). General circulation experiments with the primitive equation I the basic experiment. *Monthly Weather Review*, 91, 99-164. http://dx.doi.org/10.1175/1520-0493(1963)091<0099:GCEWTP>2.3.CO;2

Subeesh, M. P., Unnikrishnan, A. S., Fernando, V., Agarwadekar, Y., Khalap, S. T., Satelkar, N. P., & Shenoi. (2013). Observed tidal currents on the continental shelf off the west coast of India. *Continental Shelf Research*, 69, 123-140. https://doi.org/10.1016/j.csr.2013.09.008

Subeesh, M. P., & Unnikrishnan, A. S. (2016). Observed internal tides and near-inertial waves on the continental shelf and slope off Jaigarh, central west coast of India. *Journal of Marine Systems*, 157, 1-19. https://doi.org/10.1016/j.jmarsys.2015.12.005

Subeesh, M. P., Unnikrishnan, A. S., & Francis, P. A. (2021). Generation, propagation and dissipation of internal tides on the continental shelf and slope off the west coast of India. *Continental Shelf Research*, 214. https://doi.org/10.1016/j.csr.2020.104321

Tang, G., Deng, Z., Chen, R., & Xiu, F. (2023). Effects of the Kuroshio on internal tides in the Luzon Strait: A model study. Frontiers in Marine Science, 9, 995601. https://doi.org/10.3389/fmars.2022.995601

Thadathil, P., & Gosh, A. K. (1992). Surface layer temperature inversion in the Arabian Sea during winter. *Journal of Oceanography*, 48, 293–304. https://doi.org/10.1007/BF02233989

Venkatesan, R., Shamji, V. R., Latha, G., Mathew, S., Rao, R. R., Muthiah, A., & Atmanand, M. A. (2013). In situ ocean subsurface time-series measurements from OMNI buoy network in the Bay of Bengal. *Current Science*, 104(9), 1166–1177

Wunsch, C. (1975). Internal tides in the ocean. Reviews of Geophysics, 13(1), 167-182. https://doi.org/10.1029/RG013i001p00167

Xu, Z., Liu, K., Yin, B., Zhao, Z., Wang, Y., & Li, Q. (2016). Long-range propagation and associated variability of internal tides in the South China Sea. Journal of Geophysical Research: Oceans, 121(11), 8268–8286. https://doi.org/10.1002/2016JC012105

Yadidya, B., Rao, A. D., & Mohanty, S. (2021). Simulation of diurnal variability in vertical density structure using a coupled model. Scientific Reports, 11, 10916. https://doi.org/10.1038/s41598-021-90426-w

Yadidya, B., Rao, A. D., & Latha, G. (2022a). Investigation of internal tides variability in the Andaman Sea: Observations and simulations. *Journal of Geophysical Research: Oceans*, 127, e2021JC018321. https://doi.org/10.1029/2021JC018321

Yadidya, B., & Rao, A. D. (2022b). Interannual variability of internal tides in the Andaman Sea: An effect of Indian Ocean Dipole. *Scientific Reports, 12*, 11104. https://doi.org/10.1038/s41598-022-15301-8

Yadidya, B., & Rao, A.D. (2022c). Projected climate variability of internal waves in the Andaman Sea. *Commun Earth Environ* 3, 252. https://doi.org/10.1038/s43247-022-00574-8

This article is protected by copyright. All rights reserved.

Author Manuscript

Zilberman, N. V., Becker, J. M., Merrifield, M. A., & Carter, G. S. (2009). Model estimates of M_2 internal tide generation over Mid-Atlantic Ridge topography. *Journal of Physical Oceanography*, 39(10), 2635–2651. https://doi.org/10.1175/2008JPO4136.1

Mohanty, S., Rao, A. D., & Latha, G. (2018). Energetics of semidiurnal internal tides in the Andaman Sea. Journal of Geophysical Research: Oceans, 123(9), 6224–6240. https://doi.org/10.1029/2018JC013852

This article is protected by copyright. All rights reserved.